Haverford College

Haverford Scholarship

Faculty Publications

Chemistry

1997

The OBrO C(2A2)←X(2B1) absorption spectrum

Charles E. Miller
Haverford College

Scott L. Nickolaisen

Joseph S. Francisco

Stanley P. Sander

Follow this and additional works at: https://scholarship.haverford.edu/chemistry_facpubs

Charles E. Miller, Scott L. Nickolaisen, Joseph S. Francisco, and Stanley P. Sander

Additional information on J. Chem. Phys.

The OBrO $C(^2A_2)\leftarrow X(^2B_1)$ absorption spectrum

Charles E. Miller,[a)] Scott L. Nickolaisen,[b)] Joseph S. Francisco,[c)] and Stanley P. Sander

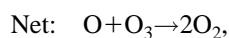*M/S 183-901, Jet Propulsion Laboratory, California Institute of Technology, Pasadena, California 91109-8099*

The highly structured visible absorption spectrum of the bromine dioxide radical, OBrO, has been observed in the 15 500–26 000 cm^{-1} region. The spectrum is dominated by a long progression in the Br–O symmetric stretching motion (ν_1') and a series of short progressions built on the bending mode (ν_2'); there are no features associated with the excitation of the antisymmetric stretching mode (ν_3'). The spectrum also contains numerous transitions originating from the (0,1,0) and (1,0,0) vibrational levels of the electronic ground state, $X(^2B_1)$. A simultaneous fit to all of the observed vibronic features yielded the frequencies $\nu_1''=799.4$ cm^{-1}, $\nu_2''=317.5$ cm^{-1}, $\omega_1'=641.5$ cm^{-1}, $\omega_2'=210.7$ cm^{-1}, and a band origin $T_0=15\,863$ cm^{-1}. Franck–Condon simulations combined with *ab initio* calculations of the four lowest OBrO doublet electronic states identify the spectrum as arising from the $C(^2A_2)\leftarrow X(^2B_1)$ electronic transition. © *1997 American Institute of Physics.* [S0021-9606(97)02731-1]
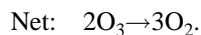
I. INTRODUCTION

The role played by halogen oxides in the formation of the polar ozone hole has been intensely investigated over the last decade.[1] The pioneering measurements of Anderson and co-workers[2] demonstrated the anticorrelation between ClO and O$_3$ concentrations in the polar stratosphere and verified the importance of the catalytic ClO$_x$ reaction cycles proposed by Molina[3]

Cycle 1:

$$Cl+O_3\rightarrow ClO+O_2 \tag{R1}$$

$$ClO+O\rightarrow Cl+O_2 \tag{R2}$$

Net: $O+O_3\rightarrow 2O_2$,

Cycle 2:

$$ClO+ClO+M\rightarrow ClOOCl+M \tag{R3}$$

$$ClOOCl+h\nu\rightarrow Cl+ClOO \tag{R4}$$

$$ClOO+M\rightarrow Cl+O_2+M \tag{R5}$$

$$Cl+O_3\rightarrow ClO+O_2 \tag{R1}$$

$$Cl+O_3\rightarrow ClO+O_2 \tag{R1}$$

Net: $2O_3\rightarrow 3O_2$.

Laboratory studies have shown that BrO$_x$ compounds participate in analogous catalytic cycles which destroy ozone even more efficiently than the ClO$_x$ cycles.[4] Thus state-of-the-art photochemical model calculations suggest that BrO$_x$ induced stratospheric ozone losses are comparable to those induced by ClO$_x$ chemistry despite the much smaller concentrations of BrO$_x$ in the polar stratosphere.[5]

With the exception of BrO, very little is known about the chemical and physical properties of the BrO$_x$ compounds. The discovery of bromine dioxide, OBrO, in the bromine sensitized photodecomposition of ozone[6–8] indicates the potential importance of higher bromine oxides in atmospheric chemistry. Therefore, we have undertaken a complete spectral characterization of OBrO as part of our program to understand stratospheric halogen oxide chemistry and its relationship to catalytic ozone depletion.[9–11] We have recently analyzed the pure rotational spectrum of OBrO and used this information to derive the molecular structure and harmonic force field.[12] In this paper we present a reinvestigation of the OBrO visible absorption spectrum augmented by Franck–Condon simulations and high level *ab initio* calculations. From the experimental and theoretical information now available, we conclude that the visible spectrum is due to the $C(^2A_2)\leftarrow X(^2B_1)$ electronic transition.

II. EXPERIMENT

The apparatus used in these experiments has been described in detail previously.[10] It consists of a 100-cm-long multipass absorption cell coupled to a 0.32-m focal length monochromator/1024-element optical multichannel analyzer. Spectra were acquired with the external White-type mirrors adjusted for eight passes (total optical path length of 720 cm) and 0.06-nm resolution (~60 nm coverage per scan). The probe light was supplied by a 150-W xenon arc lamp and data acquisition controlled via a personal computer. Temperature control was accomplished by circulating cooled methanol through a jacket which surrounds the absorption cell.

OBrO was generated by flowing molecular bromine with the products of an O$_2$/He discharge through the absorption cell at ~250 K. No OBrO features were observed while any

---

[a)]Electronic mail: cmiller@fluvs.jpl.nasa.gov; current address: Department of Chemistry, Haverford College, Haverford, PA 19041.
[b)]Also at: Department of Chemistry and Biochemistry, California State University, Los Angeles, CA 90032.
[c)]Also at: Department of Chemistry, Purdue University, West Lafayette, IN 47907-1393.

TABLE I. Transition energies and assignments for the OBrO $C(^2A_2) \leftarrow X(^2B_1)$ spectrum.[a]

n	$(n,0,0) \leftarrow$ $(0,0,0)$	$(n,1,0) \leftarrow$ $(0,0,0)$	$(n,2,0) \leftarrow$ $(0,0,0)$	$(n,0,0) \leftarrow$ $(0,1,0)$	$(n,2,0) \leftarrow$ $(0,1,0)$	$(n,0,0) \leftarrow$ $(1,0,0)$	$(n,1,0) \leftarrow$ $(1,0,0)$
0	15 863	16 078	16 290	15 546			
1	16 499	16 711	16 915	16 178		15 697	15 918
2	17 129	17 336	17 541	16 815	17 234	16 330	
3	17 748	17 958	18 160	17 437	17 852		
4	18 367	18 570	18 770	18 053	18 465		
5	18 973	19 171	19 367	18 657	19 062		
6	19 580	19 782	19 978	19 257	19 662		
7	20 183	20 379	20 575	19 858	20 262		
8	20 780	20 969	21 138	20 452	20 852		
9	21 360	21 547	21 734	21 027	21 447		
10	21 937	22 112					
11	22 502	22 684					
12	23 055	23 234					
13	23 613	23 776					
14	24 151	24 329					
15	24 687	24 858					
16	25 230	25 380					
17	25 755						

[a]All energies in cm^{-1}.

gases flowed, consistent with previous observations,[7,8] but strong OBrO signals were observed after pumping on the condensate collected on the cell walls. Helium (Air Products) and oxygen (Air Liquide) were used as received. Bromine (Fisher) was degassed prior to use.

Spectra were recorded between 280 nm and 700 nm in 60-nm segments. Individual spectra were calibrated using the absolute wavelengths of the atomic lines (in air) generated by Ar, Ne, and Hg hollow cathode lamps. The wavelength scale was then obtained from a quadratic fit of the absolute wavelengths to the OMA pixel position. This resulted in rms fitting errors of 0.01 nm or less for the calculated wavelengths of the calibration lines. The reproducibility of individual OBrO vibronic features was found to be ± 3 cm^{-1} although uncertainties within a single OMA spectrum were less than 1 cm^{-1}. The line positions reported in Table I represent an average of all observations for a given feature.

III. COMPUTATIONAL METHODS

Ab initio molecular orbital calculations for OBrO were performed with the GAUSSIAN 92 program suite.[13] All equilibrium geometries were fully optimized using Schlegel's analytical gradient method[14] at the second-order Møller–Plesset perturbation (MP2) level of theory[15] with all electrons correlated. The geometries were optimized to better than 0.1 pm for bond distances and 0.1° for bond angles. With a convergence of at least 10^{-9} on the density matrix, the rms force was less than 10^{-4} a.u. for the optimized structures. Dunning's triple zeta double polarized basis set, denoted $TZ2P$ was used for all calculations. The O-atom $TZ2P$ basis sets were composed of Dunning's $5s3p$ contraction[16] with two d-function polarization orbital exponents.[17] The Br $TZ2P$ basis set contained a $6s5p2d$ contraction of the $17s13p6d$ primitive set given by Schaefer *et al.*[18] The orbital exponents of the two d polarization func-

tions were $\alpha_d = 0.674$ and 0.225. All six components of the Cartesian d functions were included in the basis sets.

Exploratory molecular orbital calculations were performed at the MP2/$TZ2P$ level of theory. The geometries and second derivatives obtained from these calculations were then used as the initial inputs for calculations using single and double excitation coupled-cluster theory including a perturbational estimate of the effects of connected triple excitations [CCSD(T)].[19] No corrections for relativistic effects associated with the Br-atom electronic structure were included in the present calculations.

IV. RESULTS

A. Absorption spectrum and vibrational frequency analysis

An overview of the OBrO visible absorption spectrum is shown in Fig. 1. The spectrum originates below 16 000 cm^{-1}, extends to nearly 26 000 cm^{-1}, and is characterized by extensive vibronic structure. The Franck–Condon envelope is dominated by a long progression in ν_1', the Br–O symmetric stretching mode, with an average spacing of approximately 630 cm^{-1}. A short progression in the bending mode $\nu_2'(\Delta \nu \sim 210$ $cm^{-1})$ is built on each component of the ν_1' progression. This creates the intense doublet pattern observed throughout the spectrum. Line positions and transition assignments are collected in Table I.

The weaker features in each wing of the Franck–Condon envelope reveal a number of interesting characteristics. Figure 2 illustrates that the ν_1' progression contains transitions with up to 17 quanta of excitation. Even more interesting is the fact that the relative intensities of the two components within each doublet change with increasing excitation energy. The doublets are associated with the first two components of the ν_2' progression for a given value of n_1'. Below the Franck–Condon maximum, corresponding to $n \lesssim 6$, tran-
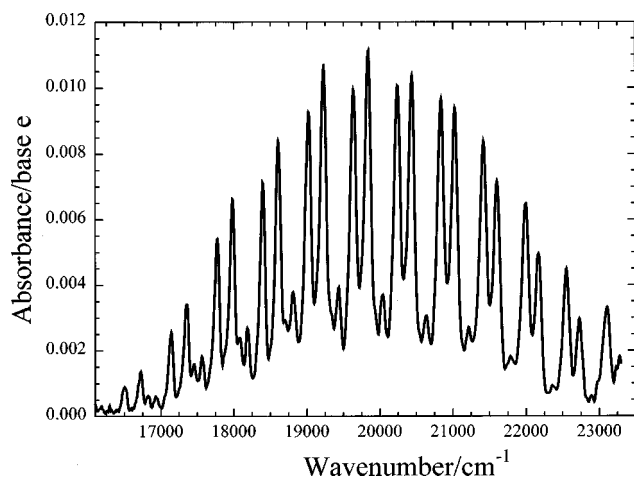
FIG. 1. An overview of the OBrO visible absorption spectrum.

FIG. 3. A detailed view of the OBrO visible absorption spectrum near the transition origin. Note the presence of numerous hot bands in addition to the features associated with the main ν_1' and ν_2' progressions.

sitions terminating in the $(n,1,0)$ vibrational levels are more intense than those which terminate in the $(n,0,0)$ levels; however, an intensity reversal occurs in the neighborhood of $n=7$ and by $n=8$ the $(8,0,0)\leftarrow(0,0,0)$ transition is more intense than the $(8,1,0)\leftarrow(0,0,0)$ transition. The intensity shift becomes more pronounced at high n where the $(n,0,0)\leftarrow(0,0,0)$ transitions dominate and the $(n,1,0)\leftarrow(0,0,0)$ features have essentially vanished.

Below 18 000 cm^{-1} the spectral intensity diminishes rapidly and a characteristic pattern of four transitions is observed for every value of n_1'. Figure 3 shows an expanded view of the extremely weak absorptions recorded near 16 000 cm^{-1}; note that the four feature pattern clearly persists. Based on the lack of a similar four feature pattern near 15 200 cm^{-1}, we assign the 15 863 cm^{-1} feature as the electronic transition origin, T_0. The features at 15 863, 16 078, and 16 290 cm^{-1} form a progression in ν_2' as evidenced by the spacings of 215 and 212 cm^{-1}, respectively. The wave number differences between these features and their counter-
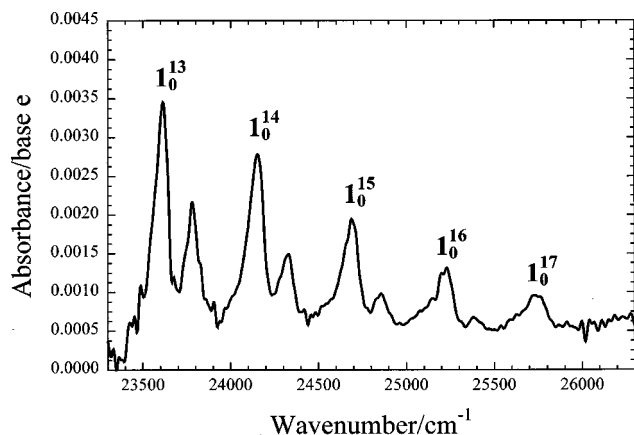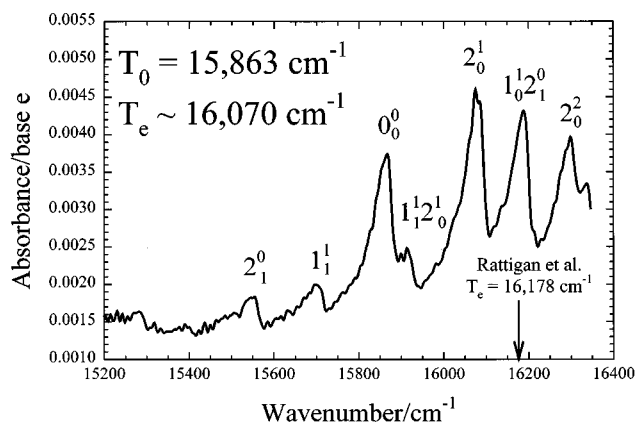

FIG. 2. An expanded view of the OBrO visible absorption spectrum at higher energies. The numbers above each transition group refer to the number of quanta in the Br–O symmetric stretching mode ν_1'. Note the change in the relative intensities of the transitions within each group when compared to the transitions in the 17 000–20 000 cm^{-1} range (Fig. 1).

parts at 16 499, 16 711, and 16 915 cm^{-1} confirm that they respresent a continuation of the main ν_1' progression. The feature at 16 178 cm^{-1} is not obviously related to the main ν_1' or ν_2' progressions, but it is separated by one quantum of ν_1' from its counterpart at 16 815 cm^{-1} as well as from the weak feature at 15 546 $^{-1}$. The 317 cm^{-1} difference between the 15 546 cm^{-1} feature and the T_0 transition is in excellent agreement with the predicted bending frequency for $X(^2B_1)$.[12] The 15 546, 16 178, 16 815, etc. transitions are thus assigned to a hot band progression originating from the first excited bending level of the electronic ground state, $X(^2B_1)(0,1,0)$. Further analysis revealed that the weak features at 15 697 and 15 918 cm^{-1} belong to a hot band progression originating from the first excited symmetric stretching level, $X(^2B_1)(1,0,0)$. Therefore, all of the observed transitions may be assigned using only the totally symmetric vibrations of the upper and lower electronic states; there is no indication of any activity in the antisymmetric stretching mode.

A simultaneous least squares fit to all of the line positions listed in Table I was performed using the expression

$$E(n_1,n_2)=T_0+n_1\omega_1+n_1^2x_{11}+n_2\omega_2+n_2^2x_{22}+n_1n_2x_{12} \tag{1}$$

for each upper state vibrational level; values for ν_1'' and ν_2'' were included for the appropriate hot band transitions. The value of T_0 was fixed to the experimental value of 15 863 cm^{-1} and the remaining constants were floated. The optimized parameters fit all 66 assigned transitions with an rms error of 6.67 cm^{-1}. The resulting values of ν_1'' and ν_2'' are collected in Table II along with the value of ν_3'' obtained from the FTIR spectrum shown in Fig. 4. This marks the first determination of the three $X(^2B_1)$ vibrational frequencies in the gas phase. No attempt was made to correct these values for anharmonicity since only transitions associated with the fundamental vibrations have been observed. In contrast, the vibrational levels of the upper electronic state sampled a

TABLE II. Vibrational frequencies (cm^{-1}) for OBrO $X(^2B_1)$.

Vibrational mode	Expt. This work	CCSD(T) This work	NCA Ref. 12	Matrix IR[a] Ref. 31	Matrix IR
ω_1	799.4	797	794.5	795.7	794.1[c]
ω_2	317.5	317	311	317.0	
ω_3	848.6	845	853	845.2	851.9[b]
					846.6[c]

[a]Values for O^{79}BrO.
[b]Reference 29.
[c]Reference 30.

TABLE III. Spectroscopic parameters (cm^{-1}) for OBrO $C(^2A_2)$.

Parameter	This work	Rattigan et al. Ref. 6	Kölm et al. Ref. 31
T_e	16 070	16 178	
T_0	15 863	16 509	16 785
ω_1	641.5	638	631
ω_2	210.7	~200	221
χ_{11}	−3.52	−3.58	
χ_{22}	1.09	⋯	
χ_{12}	−2.70	⋯	

wide range of quantum numbers. This enabled us to determine harmonic vibrational frequencies and anharmonicity corrections for ν_1' and ν_2'; the results for the excited state are gathered in Table III.

B. Ab initio results

Submillimeter spectroscopy has confirmed that, like OClO,[20] the OBrO electronic ground state possesses C_{2v} symmetry and a $^2B_1$ electronic configuration.[12] The optimized minimum energy CCSD(T)/$TZ2P$ structure for OBrO also possesses a $^2B_1$ electronic configuration, consistent with the experimental findings. In this structure, the 51 electrons of OBrO are distributed among 26 molecular orbitals ($14a_1$, $3a_2$, $7b_1$, and $2b_2$ orbitals) with the configuration

Core...$(14a_1)^2(2b_2)^2(3a_2)^2(7b_1)^1$,

where $7b_1$ is a p_x orbital perpendicular to the molecular plane. The calculated and experimental structures {CCSD(T): $R_{Br-O}=166.0$ pm, $\theta_{OBrO}=114.8°$; Expt.:

$R_{Br-O}=164.91$ pm, $\theta_{OBrO}=114.44°$ (Table IV)} are in excellent agreement as are the vibrational frequencies {CCSD(T): $\omega_1=797$ cm^{-1}, $\omega_2=317$ cm^{-1}, $\omega_3=845$ cm^{-1}; Expt.: $\nu_1=799.4$ cm^{-1}, $\nu_2=317.5$ cm^{-1}, $\nu_3=848.6$ cm^{-1} (Table II)}. These results suggest that the CCSD(T)/$TZ2P$ wavefunctions provide a faithful representation of the radical, even without relativistic corrections, and that we may have confidence in the accuracy of other calculated molecular properties.

Another major objective of the ab initio calculations was to aid in the identification of the upper electronic state in the OBrO visible absorption spectrum. The calculations identified three low-lying electronic states—$A(^2B_2)$, $B(^2A_1)$, and $C(^2A_2)$—created by singlet excitations from the $3a_2$, $2b_2$, and $14a_1$ orbitals into the singly occupied $7b_1$ orbital. An analogous set of excited electronic states with the same symmetries and similar energy separations was calculated for OClO.[21] The optimized geometry for each state was checked to verify that it was a true minimum on the OBrO potential energy surface by performing vibrational frequency calculations at the MP2/$TZ2P$ level with analytical second derivatives.[22] The geometries for the three low-lying excited states are given in Table IV.

The $A(^2B_2)$ electronic state is predicted to be strongly bent with a valence angle of 85.6°. We estimate the adiabatic $A \leftarrow X$ transition energy to be $T_e=12\,850$ cm^{-1}. The $B \leftarrow X$ and $C \leftarrow X$ adiabatic transition energies are nearly isoenergetic with predicted T_e values of 16 335 and 16 760 cm^{-1}, respectively. Peterson and Werner[21] found similar results for OClO where the $B \leftarrow X$ and $C \leftarrow X$ adiabatic transitions exhibit a separation of ca. 161 cm^{-1} at the CMRCI

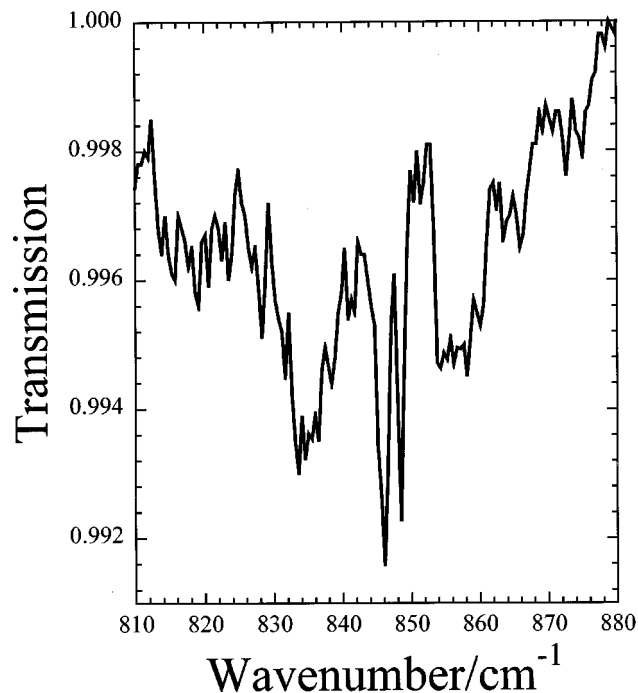

FIG. 4. A moderate resolution FTIR spectrum of the OBrO ν_3 band. The pair of sharp Q branches at 846.3 and 848.6 cm^{-1} are due to the O^{81}BrO and O^{79}BrO isotopomers, respectively.

TABLE IV. Geometries and relative energies for low-lying doublet electronic states of OBrO calculated at the CCSD(T)/$TZ2P$ level of theory.

State	Geometry[a] R_{Br-O}/pm	θ_{O-Br-O}/deg	T_e/cm^{-1}
$X(^2B_1)$	166.0	114.8	0
$A(^2B_2)$	175.9	85.6	12 580
$B(^2A_1)$	177.5	118.1	16 335
$C(^2A_2)$	178.5	103.2	16 760
Expt. $X(^2B_1)$ (Ref. 12)	164.9	114.4	0
Expt. "A" (This work)	175.9±1.0	104.4±0.5	16 070

[a]Excited state energies calculated relative to the $X(^2B_1)$ state energy of −2722.678 53 hartrees.

TABLE V. Calculated rotational constants (MHz) for OBrO in various low-lying electronic states.

Rotational constant	Electronic state			
	$X(^2B_1)$	$A(^2B_2)$	$B(^2A_1)$	$C(^2A_2)$
A	27 784.4786	13 326.9128	26 701.3832	18 052.0287
B	8070.5381	11 052.0592	6812.3378	8073.4144
C	6253.9559	6041.6752	5427.5932	5578.5277

$(3d2f1g)$ level of theory. Excitations into the $B(^2A_1)$ and $C(^2A_2)$ states involve large and nearly identical increases in the Br–O bond length, 11.5 and 12.5 pm, respectively, but the $B(^2A_1)$ bond angle *increases* 2.3° to 118.1° while the $C(^2A_2)$ bond angle *decreases* 11.6° to 103.2°. This behavior was also observed in the OClO calculations where the $B(^2A_1)$ and $C(^2A_2)$ states had similar bond lengths, but differed by 13.6° in bond angle.[21]

The resolution of the spectrometer used in these studies was insufficient to resolve any rotational structure in the vibronic transitions, but extensive rotational structure has been observed in the electronic absorption spectrum of OClO.[23–25] Inspection of the vibronic features in Fig. 3 shows red-degraded contours reminiscent of those observed for lower resolution spectra of OClO at lower transition energies.[25] The strength of the OBr–O bond is unknown so we cannot calculate the dissociation threshold, but it seems likely that the OBrO visible absorption spectrum will contain rotational structure which has not been rendered competely unresolvable by predissociative broadening. Therefore, in Table V we present the rotational constants for each of the low-lying doublet electronic states calculated from the optimized CCSD(T)/$TZ2P$ structures as a guide for future spectral analysis.

V. DISCUSSION

The existence of the OBrO radical in the gas phase had been disputed despite its identification in a magnetically deflected molecular beam,[26] in solution,[27,28] and in cryogenic matrices (IR[29–31] and ESR[32]). Then in 1994 Rattigan *et al.* observed a highly structured visible absorption spectrum during the bromine-sensitized photodecomposition of ozone.[6] The striking resemblance of this spectrum to the OClO $C(^2A_2)\leftarrow X(^2B_1)$ absorption spectrum[25] led Rattigan *et al.* to hypothesize that they had observed the signature of OBrO. We have now conclusively demonstrated that OBrO is the carrier of the 15 500–26 000 cm^{-1} spectrum shown in Fig. 1 by recording the visible, submillimeter[12] and infrared (Fig. 4) spectra of OBrO under identical experimental conditions.

The assignments provided in Table I include 21 transitions which occur from vibrationally excited levels of the $X(^2B_1)$ electronic state: 18 which originate from (0,1,0) and three which originate in the (1,0,0) level. Values of ν_1'' =799.4 cm^{-1} and ν_2''=317.5 cm^{-1} were derived from a simultaneous least squares fit to all of the transitions given in Table I. These frequencies combined with the ν_3'' =848.6 cm^{-1} value obtained for O^{79}BrO from the infrared

spectrum (Fig. 4) constitute the complete set of fundamental vibrational frequencies for gas phase OBrO $X(^2B_1)$. These values are compared in Table II with the vibrational frequencies from our CCSD(T) calculations, harmonic force field calculations,[12] and matrix isolation infrared measurements;[29–31] the overall agreement is excellent. The fact that the *ab initio* calculations reproduce the experimental frequencies so well indicates that the calculated $X(^2B_1)$ potential energy surface is extremely accurate in the neighborhood of the equilibrium geometry. The excellent agreement among all of the different determinations of the vibrational frequencies further supports the present assignments.

The increased detection sensitivity of our experimental apparatus has enabled us to resolve weak features in the 15 000–16 500 cm^{-1} range which Rattigan *et al.*[6] were unable observe. This new spectral information, including all of the features in Fig. 3, shows that the origin of the OBrO visible absorption spectrum is 15 863 cm^{-1} and that the 16 499-cm^{-1} feature (16 509 cm^{-1} in Ref. 6) assigned by Rattigan *et al.* as the origin transition is actually the $(1,0,0)\leftarrow(0,0,0)$ transition. From the experimentally determined ω_1' and ω_2' and an estimate of 700 cm^{-1} for ω_3', we obtain a zero point energy of approximately 776 cm^{-1} for the excited state. Combining this value with T_0 and a value of 982.8 cm^{-1} calculated for the $X(^2B_1)$ zero point energy, one obtains $T_e\sim$ 16 070 cm^{-1}.[33]

There is now sufficient information available to determine the identity of the electronic transition which gives rise to the OBrO visible absorption spectrum. Submillimeter spectra of the OBrO rotational spectrum have revealed that the electronic ground state has a $^2B_1$ electronic configuration. The CCSD(T) calculations reported in Table IV predicted a $X(^2B_1)$ configuration as well as three possibilities for the excited electronic state. We can immediately reject $A(^2B_2)$ as the upper electronic state since the calculated transition energy is 4000 cm^{-1} too low and the $A(^2B_2)\leftarrow X(^2B_1)$ transition is electric dipole forbidden. The 16 335 and 16 769 cm^{-1} adiabatic energies calculated for the $B(^2A_1)\leftarrow X(^2B_1)$ and $C(^2A_2)\leftarrow X(^2B_1)$ transitions are in reasonable agreement with the experimental T_e value, and both transitions are allowed under electric dipole selection rules. Transitions to both states are predicted to involve the large increases in the Br–O bond lengths implied by the extended ν_1' progression in the spectrum. The bond angle changes calculated for each state are also consistent with the observed progressions in ν_2'.

To achieve a definite assignment we calculated a series of Franck–Condon factor (FCF) spectral simulations.[34] These simulations required a Br–O bond length increase of (11.0±1.0) pm and a bond angle decrease of 10.0°±0.5° in the excited electronic state to obtain agreement with the experimental intensity distribution. From these structural changes and the known ground state geometry, we estimate the upper state geometry as R_{Br-O}=(175.9±1.0) pm and θ_{OBrO}=104.4°±0.5°. The FCF simulations also demonstrated that the relative intensities of the $(n,1,0)\leftarrow(0,0,0)$ and $(n,0,0)\leftarrow(0,0,0)$ progressions could not be reproduced without the inclusion of Duschinsky rotation. This intensity
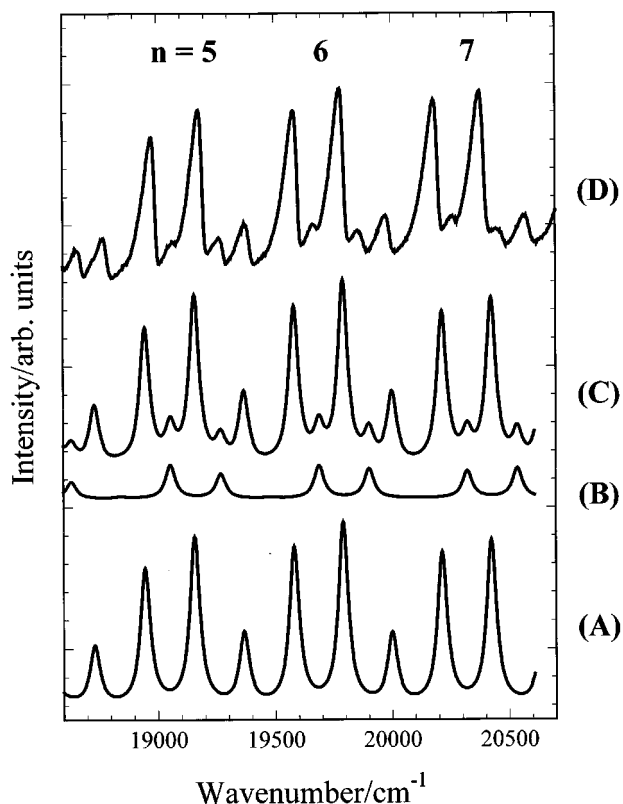
FIG. 5. A detailed view of the Franck–Condon simulation of the OBrO absorption spectrum in the region of maximum absorbance. The numbers above each transition group refer to the number of quanta in ν_1'. Trace A: Transitions originating in the (0,0,0) level of $X(^2B_1)$. The simulation is restricted to modes ν_1' and ν_2' only. Trace B: Franck–Condon simulation of the transitions arising from the $X(^2B_1)(0,1,0)$ level. The intensities have been scaled by the Boltzman factor corresponding to the experimental temperature (260 K). Trace C: The sum of traces A and B. Trace D: The experimental OBrO absorption spectrum.

FIG. 6. The complete OBrO $C(^2A_2) \leftarrow X(^2B_1)$ Franck–Condon simulation. Compare to the experimental absorption spectrum in Fig. 1.

information proved valuable in locating the best simulation geometries. The molecular structure and energy calculated for the $C(^2A_2)$ state are in excellent agreement with our experimental observations, therefore we assign the OBrO visible spectrum to the $C(^2A_2) \leftarrow X(^2B_1)$ electronic transition.

Figure 5 shows the optimized FCF simulation in the region of the Franck–Condon maximum. Trace A illustrates that transitions originating only from the $X(^2B_1)(0,0,0)$ vibrational level are insufficient to account for all of the observed features. The addition of hot band transitions from the $X(^2B_1)(0,1,0)$ level resulted in a total simulation, Trace C, which reproduces the experimental spectrum very well. An inspection of Trace B shows that only transitions from $X(^2B_1)(0,1,0)$ to $C(^2A_2)$ levels with an even number of quanta in the ν_2' mode have significant intensity. This was a particularly satisfying triumph of the FCF simulations since no $C(^2A_2)(n,1,0) \leftarrow X(^2B_1)(0,1,0)$ transitions were assigned during the frequency analysis. The complete FCF simulation is shown in Fig. 6.

The spectra reported here were unable to resolve rotational structure in any of the observed vibronic features;
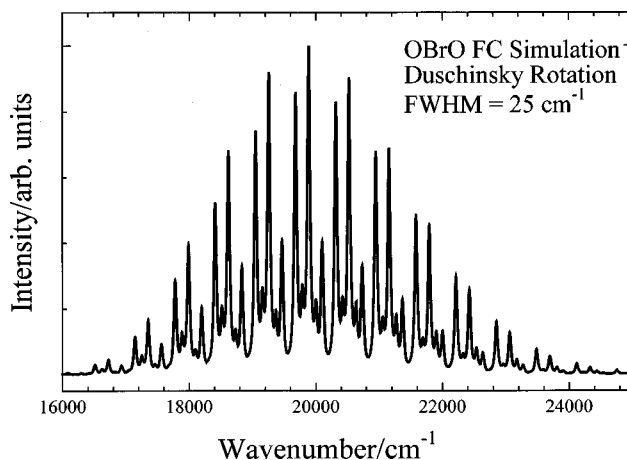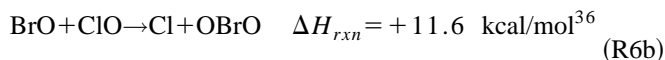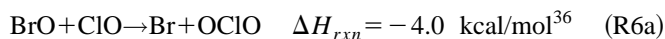
however, it seems likely that some rotational structure will escape predissociative broadening, especially for lower energy transitions. It will be straightforward to confirm the present transition assignments should rotationally resolved spectra become available. Ground state combination differences evaluated from these spectra could be compared against the known rotational constants for $X(^2B_1)(0,0,0)$ and $(0,1,0)$ to verify the hot band assignments. An examination of the rotational constants given in Table V shows that it will also prove straightforward to confirm the identity of the upper electronic state from its rotational constants since the A and $(B+C)/2$ values for $C(^2A_2)$ are very different from those of the nearly isoenergetic $B(^2A_1)$ state.

We have been unable to generate sufficient number densities of OBrO to perform an NO titration and obtain absolute absorption cross sections; however, we estimate that the cross sections of the intense features near 20 000 cm^{-1} are on the order of $(1.5\pm1.0)\times10^{-17}$ cm^2 molecule^{-1}. This would be consistent with the magnitude of the OClO cross sections and implies that the spectra in Figs. 1 and 4 were recorded with number densities on the order of 1 $\times10^{13}$ molecules cm^{-3}. Given the manner in which all other molecular properties of OBrO have been accurately predicted based on the properties of OClO, it seems very unlikely that the actual OBrO absorption cross sections deviate from this estimate.

The role of the OBrO radical in atmospheric ozone depletion will be determined by its source chemistry, which is poorly defined at this time. The BrO+ClO reaction has been identified as the principal source of OClO in the polar stratosphere,[35] but high

$$BrO+ClO \rightarrow Br+OClO \quad \Delta H_{rxn} = -4.0 \text{ kcal/mol}^{36} \quad \text{(R6a)}$$

$$BrO+ClO \rightarrow Cl+OBrO \quad \Delta H_{rxn} = +11.6 \text{ kcal/mol}^{36} \quad \text{(R6b)}$$

level *ab initio* calculations predict that the endothermic channel (R6b) will not be important at stratospheric temperatures

($\sim$220 K). Rawley *et al.*[8] have shown that source reaction BrO+O$_3$ has a large activation energy and will also be negligible at stratospheric temperatures. Both recent investigations of the BrO+BrO reaction[7,8] have demonstrated that OBrO is formed in the Br$_2$/O$_3$/$h\nu$ system, but that it is not a primary reaction product. The peculiar source chemistry employed in the present experiments strongly suggest that an efficient heterogeneuos mechanism exists which converts BrO into an adsorbed compound, probably a higher bromine oxide, which then thermally decomposes to yield gas phase OBrO. Therefore, we hypothesize that if OBrO is present at chemically significant levels in the atmosphere, then its source chemistry is probably heterogeneous.

An estimate of $\int J(\lambda)d\lambda$ suggests that the atmospheric lifetime of OBrO is on the order of seconds during daylight hours and that OBrO will exist in a photochemical steady state. If formed at night by a heterogeneous mechanism, then its principal impact will be as a temporary BrO reservoir. A more quantitative assessment of its atmospheric importance awaits *in situ* detection and a better identification of the source chemistry.

VI. CONCLUSIONS

An experimental and theoretical analysis of the OBrO $C(^2A_2) \leftarrow X(^2B_1)$ absorption spectrum has been presented. A complete set of $X(^2B_1)$ vibrational frequencies have been determined for the gas phase molecule as have values for $T_0(C(^2A_2))$, ω_1', ω_2' and their anharmonic corrections. A Franck–Condon analysis of the spectrum combined with the structural information available from submillimeter spectroscopy allowed us to obtain a structure for the upper electronic state which was in good agreement with the $C(^2A_2)$ structure calculated at the CCSD(T)/$TZ2P$ level of theory. The information accumulated on OBrO to date suggests that its properties may be well estimated from the appropriate periodic adjustments to the properties of OClO.

Note added in proof. Since the completion of this work, Pacios and Gomez have reported UMP2 and CCSD(T) calculations on OBrO $X(^2B_1)$ using the AREF/$TZ(2df)$ basis set.[37] Their CCSD(T) geometry {$R_{Br-O}=165.0$ pm, $\theta_{OBrO} = 114.9°$} is in good agreement with experiment and the CCSD(T)/$TZ2P$ geometry reported in Table III. However, their UMP2/AREP/$TZ(2df)$ vibrational frequencies {$\omega_1 = 897$ cm^{-1}, $\omega_2 = 328$ cm^{-1}, $\omega_3 = 939$ cm^{-1}} deviate by 12.3%, 3.5%, and 10.7% from the experimental values, while our vibrational frequencies calculated at the CCSD(T)/$TZ2P$ level of theory are essentially indistinguishable from the experimental values.

ACKNOWLEDGMENTS

[1] Scientific Assessment of Ozone Depletion: 1994, WMO Global Ozone Research and Monitoring Project, Report No. 37, 1994.

[2] J. G. Anderson, W. H. Brune, and M. H. Profitt, J. Geophys. Res. **94**, 11 465 (1989).

[3] M. J. Molina, Angew. Chem. Int. Ed. Engl. **35**, 1778 (1996), and references therein; M. J. Molina, Angew. Chem. **108**, 1900 (1996).

[4] S. P. Sander and R. T. Watson, J. Phys. Chem. **85**, 4000 (1981).

[5] P. O. Wennberg, R. C. Cohen, R. M. Stimpfle, J. P. Koplow, J. G. Anderson, R. J. Salawitch, D. W. Fahey, E. L. Woodbridge, E. R. Keim, R. S. Gao, C. R. Webster, R. D. May, D. W. Toohey, L. M. Avallone, M. H. Proffitt, M. Loewnestein, J. R. Podolske, K. R. Chan, and S. C. Woofsy, Science **226**, 398 (1994).

[6] O. V. Rattigan, R. L. Jones, and R. A. Cox, Chem. Phys. Lett. **230**, 121 (1994).

[7] O. V. Rattigan, R. A. Cox, and R. L. Jones, J. Chem. Soc. Faraday Trans. **91**, 4189 (1995).

[8] D. M. Rawley, M. H. Harwood, R. A. Freshwater, and R. L. Jones, J. Phys. Chem. **100**, 3020 (1996).

[9] S. P. Sander, R. R. Friedl, and J. S. Francisco in *Atmospheric Chemistry*, edited by J. Barker (World Scientific, Singapore, 1995).

[10] S. L. Nickolaisen, R. R. Friedl, and S. P. Sander, J. Phys. Chem. **98**, 155 (1994).

[11] M. Birk, R. R. Friedl, E. A. Cohen, H. M. Pickett, and S. P. Sander, J. Chem. Phys. **91**, 6588 (1989).

[12] H. S. P. Müller, C. E. Miller, and E. A. Cohen, Angew. Chem. Int. Ed. Engl. **35**, 2129 (1996); H. S. P. Müller, C. E. Miller, and E. A. Cohen, Angew. Chem. **108**, 2285 (1996).

[13] M. J. Frisch, G. W. Trucks, M. Head-Gordon, P. M. W. Gill, M. W. Wong, J. B. Foresman, B. G. Johnson, H. B. Schlegel, M. A. Robb, E. S. Replogle, R. Gomperts, J. L. Andres, K. Raghavachari, J. S. Binkley, C. Gonzalez, R. L. Martin, D. J. Fox, D. J. DeFrees, J. Baker, J. J. P. Stewart, and J. A. Pople, GAUSSIAN 92, Revision C, Gaussian Inc., Pittsburgh, PA, 1992.

[14] H. B. Schlegel, J. Comput. Chem. **3**, 214 (1982).

[15] R. Krishnan and J. A. Pople, Int. J. Quantum Chem. Quantum Chem. Symp. **14**, 91 (1980).

[16] T. H. Dunning, J. Chem. Phys. **55**, 716 (1971).

[17] T. H. Dunning, J. Chem. Phys. **90**, 1007 (1989).

[18] A. Schaefer, C. Huber, and R. Ahlrichs, J. Chem. Phys. **100**, 5829 (1994).

[19] T. J. Lee and A. P. Rendell, J. Chem. Phys. **94**, 6219 (1991).

[20] R. F. Curl, R. F. Heidelberg, and J. L. Kinsey, Phys. Rev. **125**, 1993 (1962).

[21] K. A. Peterson and H.-J. Werner, J. Chem. Phys. **96**, 8948 (1992).

[22] J. A. Pople, R. Krishnan, H. B. Schlegel, and J. S. Binkley, Int. J. Quantum Chem. Quantum Chem. Symp. **13**, 225 (1979).

[23] J. B. Coon, J. Chem. Phys. **14**, 665–685 (1946).

[24] Y. Hamada, A. J. Merer, S. Michielsen, and S. A. Rice, J. Mol. Spectrosc. **86**, 499 (1981).

[25] E. C. Richard and V. Vaida, J. Chem. Phys. **94**, 153 (1991), and references therein.

[26] N. I. Butovskaya, I. L. Morosov, V. L. Tal'Rose, and E. S. Vasiliev, Chem. Phys. **79**, 21 (1983).

[27] G. V. Buxton and F. S. Dainton, Proc. R. Soc. A **304**, 427 (1968).

[28] H. D. Försterling, H. J. Lamberg, and H. Schreiber, Z. Naturforsch. **35a**, 1354 (1980); H. D. Försterling and S. Murányi, Z. Naturforsch. **35a**, 1354 (1990).

[29] D. E. Tevault, N. Walker, R. R. Smardzewski, and W. B. Fox, J. Phys. Chem. **82**, 2733 (1978).

[30] G. Maier and A. Bothur, Z. Anorg. Chem. **621**, 743 (1995).

[31] J. Kölm, A. Engdahl, O. Schrems, and B. Nelander, Chem. Phys. **214**, 313 (1997).

[32] J. R. Byberg, J. Chem. Phys. **84**, 6204 (1986); J. R. Byberg, J. Chem. Phys. **85**, 4790 (1986).

[33] Rattigan *et al.* (Ref. 6) assign their 16 509-cm^{-1} feature as the 0←0 transition and report a value of 16 178 cm^{-1} for $\nu_{0,0,0}$. This apparently represents an attempt to calculate the minimum energy of the $C(^2A_2)$ state

relative to $X(^2B_1)(0,0,0)$. Using the 638-, 200-, and 700-cm^{-1} vibrational frequencies of given in their paper, one estimates a zero point energy of 769 cm^{-1} for the excited state. When combined with their T_0 value of 16 509 cm^{-1} and the $X(^2B_1)$ zero point energy of 982.8 cm^{-1} obtained in the present study, one obtains $T_e = 16\ 723$ cm^{-1}.

[34] M. Yamaguchi, T. Momose, and T. Shida, J. Chem. Phys. **93**, 4211 (1990).

[35] A. Wahner and C. Schiller, J. Geophys. Res. **97**, 8047 (1995).

[36] J. S. Francisco (unpublished).

[37] L. F. Pacios and P. C. Gomez, J. Phys. Chem. **101**, 1767 (1997).